

Omnidirectional, polarization-independent, ultra-broadband metamaterial perfect absorber using field-penetration and reflected-wave-cancellation

Yan Kai Zhong,¹ Yi-Chun Lai,² Ming-Hsiang Tu,¹ Bo-Ruei Chen,¹ Sze Ming Fu,¹ Peichen Yu,² and Albert Lin^{1,*}

¹Department of Electronic Engineering, National Chiao-Tung University, Hsinchu, 30010, Taiwan

²Department of Photonics, National Chiao-Tung University, Hsinchu, 30010, Taiwan

*hdt65746@gmail.com

Abstract: In this work, we present the result of nickel (Ni)-based metamaterial perfect absorbers (MPA) with ultra-broadband close-to-one absorbance. The experimental broadband characteristic is significantly improved over the past effort on metamaterial perfect absorbers. An in-depth physical picture and quantitative analysis is presented to reveal the physical origin of its ultrabroadband nature. The key constituent is the cancellation of the reflected wave using ultra-thin, moderate-extinction metallic films. The ultra-thin metal thickness can reduce the reflection as the optical field penetrates through the metallic films. This leads to minimal reflection at each ultra-thin metal layer, and light is penetrating into the Ni/SiO₂ stacking. More intuitively, when the layer thickness is much smaller than the photon wavelength, the layer is essentially invisible to the photons. This results in absorption in the metal thin-film through penetration while there is minimal reflection by the metal film. More importantly, the experimental evidence for omni-directionality and polarization-insensitivity are established for the proposed design. Detailed measurement is conducted. Due to the ultrathin metal layers and the satisfactory tolerance in dielectric thickness, the broadband absorption has minimal degradation at oblique incidence. Such a wide angle, polarization-insensitive, ultra-broadband MPA can be very promising in the future, and the optical physics using sub-skin-depth metal film can also facilitate miniaturized high-performance nano-photonic devices.

©2016 Optical Society of America

OCIS codes: (040.5350) Photovoltaic; (160.3918) Metamaterials; (310.6845) Thin film devices and applications.

References and links

1. Y. Ra'di, C. R. Simovski, and S. A. Tretyakov, "Thin perfect absorbers for electromagnetic waves: theory, design, and realizations," *Phys. Rev. Appl.* **3**(3), 037001 (2015).
2. C. M. Watts, X. Liu, and W. J. Padilla, "Metamaterial electromagnetic wave absorbers," *Adv. Mater.* **24**(23), OP98–OP181 (2012).
3. Y. Cui, K. H. Fung, J. Xu, H. Ma, Y. Jin, S. He, and N. X. Fang, "Ultrabroadband light absorption by a sawtooth anisotropic metamaterial slab," *Nano Lett.* **12**(3), 1443–1447 (2012).
4. K. Aydin, V. E. Ferry, R. M. Briggs, and H. A. Atwater, "Broadband polarization-independent resonant light absorption using ultrathin plasmonic super absorbers," *Nat. Commun.* **2**, 517 (2011).
5. H. Tao, C. M. Bingham, D. Pilon, K. Fan, A. C. Strikwerda, D. Shrekenhamer, W. J. Padilla, X. Zhang, and R. D. Averitt, "A dual band terahertz metamaterial absorber," *J. Phys. D Appl. Phys.* **43**(22), 225102 (2010).
6. X. Liu, T. Starr, A. F. Starr, and W. J. Padilla, "Infrared spatial and frequency selective metamaterial with near-unity absorbance," *Phys. Rev. Lett.* **104**(20), 207403 (2010).
7. N. Liu, M. Mesch, T. Weiss, M. Hentschel, and H. Giessen, "Infrared perfect absorber and its application as plasmonic sensor," *Nano Lett.* **10**(7), 2342–2348 (2010).
8. Q. Y. Wen, H. W. Zhang, Y. S. Xie, Q. H. Yang, and Y. L. Liu, "A dual-band terahertz metamaterial based on a hybrid h-shaped cell," *Appl. Phys. Lett.* **95**, 241111 (2009).

9. H. Tao, N. I. Landy, C. M. Bingham, X. Zhang, R. D. Averitt, and W. J. Padilla, "A metamaterial absorber for the terahertz regime: design, fabrication and characterization," *Opt. Express* **16**(10), 7181–7188 (2008).
10. H. Tao, C. M. Bingham, A. C. Strikwerda, D. Pilon, D. Shrekenhamer, N. I. Landy, K. Fan, X. Zhang, W. J. Padilla, and R. D. Averitt, "Highly flexible wide angle of incidence terahertz metamaterial absorber: design, fabrication, and characterization," *Phys. Rev. B* **78**(24), 241103 (2008).
11. Y. K. Zhong, S. M. Fu, N. P. Ju, M. Tu, B. Chen, and A. Lin, "Fully planarized perfect metamaterial absorbers with no photonic nanostructures," *IEEE Photonics J.* **8**(1), 2200109 (2016).
12. V. Rinnerbauer, A. Lenert, D. M. Bierman, Y. X. Yeng, W. R. Chan, R. D. Geil, J. J. Senkevich, J. D. Joannopoulos, E. N. Wang, M. Soljačić, and I. Celanovic, "Metallic photonic crystal absorber-emitter for efficient spectral control in high-temperature solar thermophotovoltaics," *Adv. Energy Mater.* **4**(13), 1400334 (2014).
13. Y. Nam, Y. X. Yeng, A. Lenert, P. Bermel, I. Celanovic, M. Soljačić, and E. N. Wang, "Solar thermophotovoltaic energy conversion systems with two-dimensional tantalum photonic crystal absorbers and emitters," *Sol. Energ. Mat.* **122**, 287–296 (2014).
14. J. B. Chou, Y. X. Yeng, A. Lenert, V. Rinnerbauer, I. Celanovic, M. Soljačić, E. N. Wang, and S.-G. Kim, "Design of wide-angle selective absorbers/emitters with dielectric filled metallic photonic crystals for energy applications," *Opt. Express* **22**(S1 Suppl 1), A144–A154 (2014).
15. C. Argyropoulos, K. Q. Le, N. Mattiucci, G. D'Aguzzo, and A. Alu, "Broadband absorbers and selective emitters based on plasmonic Brewster metasurfaces," *Phys. Rev. B* **87**(20), 205112 (2013).
16. C. Wu, B. Neuner III, J. John, A. Milder, B. Zollars, S. Savoy, and G. Shvets, "Metamaterial-based integrated plasmonic absorber/emitter for solar thermo-photovoltaic systems," *J. Opt.* **14**(2), 024005 (2012).
17. J. Hao, J. Wang, X. Liu, W. J. Padilla, L. Zhou, and M. Qiu, "High performance optical absorber based on a plasmonic metamaterial," *Appl. Phys. Lett.* **96**(25), 251104 (2010).
18. Y. Avitzour, Y. A. Urzhumov, and G. Shvets, "Wide-angle infrared absorber based on a negative-index plasmonic metamaterial," *Phys. Rev. B* **79**(4), 045131 (2009).
19. W. H. Emerson, "Electromagnetic wave absorbers and anechoic chambers through the years," *IEEE Trans. Antenn. Propag.* **21**(4), 484–490 (1973).
20. A. Poddubny, I. Iorsh, P. Belov, and Y. Kivshar, "Hyperbolic metamaterials," *Nat. Photonics* **7**(12), 948–957 (2013).
21. M. Noginov, M. Lapine, V. Podolskiy, and Y. Kivshar, "Focus issue: hyperbolic metamaterials," *Opt. Express* **21**(12), 14895–14897 (2013).
22. C. Battaglia, C.-M. Hsu, K. Söderström, J. Escarré, F. J. Haug, M. Charrière, M. Boccard, M. Despeisse, D. T. Alexander, M. Cantoni, Y. Cui, and C. Ballif, "Light trapping in solar cells: can periodic beat random?" *ACS Nano* **6**(3), 2790–2797 (2012).
23. W. E. I. Sha, W. C. H. Choy, and W. C. Chew, "Angular response of thin-film organic solar cells with periodic metal back nanostrips," *Opt. Lett.* **36**(4), 478–480 (2011).
24. U. W. Paetzold, E. Moulin, B. E. Pieters, R. Carius, and U. Rau, "Design of nanostructured plasmonic back contacts for thin-film silicon solar cells," *Opt. Express* **19**(S6 Suppl 6), A1219–A1230 (2011).
25. S.-M. Fu, Y.-K. Zhong, and A. Lin, "An ultra-efficient energy transfer beyond plasmonic light scattering," *J. Appl. Phys.* **116**(18), 183103 (2014).
26. K. Q. Le, A. Abass, B. Maes, P. Bienstman, and A. Alù, "Comparing plasmonic and dielectric gratings for absorption enhancement in thin-film organic solar cells," *Opt. Express* **20**(S1), A39–A50 (2012).
27. A. Basch, F. J. Beck, T. Söderström, S. Varlamov, and K. R. Catchpole, "Combined plasmonic and dielectric rear reflectors for enhanced photocurrent in solar cells," *Appl. Phys. Lett.* **100**(24), 243903 (2012).
28. M. Yang, Z. Fu, F. Lin, and X. Zhu, "Incident angle dependence of absorption enhancement in plasmonic solar cells," *Opt. Express* **19**(S4 Suppl 4), A763–A771 (2011).
29. F. J. Beck, S. Mookapati, and K. R. Catchpole, "Light trapping with plasmonic particles: beyond the dipole model," *Opt. Express* **19**(25), 25230–25241 (2011).
30. S. Pillai and M. A. Green, "Plasmonics for photovoltaic applications," *Sol. Energ. Mat. Sol.* **94**(9), 1481–1486 (2010).
31. A. C. Jones, R. L. Olmon, S. E. Skrabalak, B. J. Wiley, Y. N. Xia, and M. B. Raschke, "Mid-IR plasmonics: near-field imaging of coherent plasmon modes of silver nanowires," *Nano Lett.* **9**(7), 2553–2558 (2009).
32. J. D. Joannopoulos, S. G. Johnson, R. D. Meade, and J. N. Winn, *Photonic Crystal: Molding the Flow of Light*, 2nd ed. (Princeton University, 2008).
33. Rsoft, *Rsoft CAD User Manual*, 8.2 ed. (Rsoft Design Group, 2010).
34. D. K. Cheng, *Field and Wave Electromagnetics*, 2nd ed. (Addison-Wesley, 1989).
35. S. L. Chuang, *Physics of Photonic Devices (Wiley Series in Pure and Applied Optics)*, 2nd ed. (Wiley, 2009).
36. J. Zhou, A. F. Kaplan, L. Chen, and L. J. Guo, "Experiment and theory of the broadband absorption by a tapered hyperbolic metamaterial array," *ACS Photonics* **1**(7), 618–624 (2014).
37. D. Ji, H. Song, X. Zeng, H. Hu, K. Liu, N. Zhang, and Q. Gan, "Broadband absorption engineering of hyperbolic metafilm patterns," *Sci. Rep.* **4**, 4498 (2014).

1. Introduction

Broadband or narrowband perfect absorption is important for many photonic applications [1–19]. The previous effort includes hyperbolic metamaterial tapers [3, 20, 21], metallic nanocones [15], plasmonic absorbers [4, 17], quasi-guided mode resonances in metal-dielectric-

metal cavities [17], a composite metallic grating with multiple periodicities and filling factors [8], etc. Essentially, the narrowband perfect absorption is relatively easy to implement due to the fact that the confinement of photons at a specific wavelength can be achieved using various optical phenomena. These include guided mode resonances [2, 6, 17, 22–24], plasmonic resonances [25–31], slow-light absorption enhancement, photonic density of states (PDOS) engineering in periodic structures [32]. On the other hand, the ultrabroadband absorption can be challenging in the aspect that it is difficult to find an optical phenomenon that can exist consistently over a broad spectral range and contribute to a broadband absorption. Additionally, omni-directionality and polarization independence are even more challenging aspects. In our recent publications [11], we show that the field penetration can be an important physical phenomenon that can push forward the progress of metamaterial perfect absorbers (MPAs). The decent performance is reflected in its close-to-unity absorption over a very wide spectral range, with wavelength scalability. The additional advantage is in the fully planarized nature where the lithography and etching is totally unnecessary. In our past effort, Ti-based MPAs are used to demonstrate the concept. Due to the fabrication using electron-gun (e-gun) evaporators, the thickness control of Ti thin-film at an ultra-thin thickness presents some difficulty. In this study, we use nickel (Ni)-based MPAs to show that the absorbance can actually be very close to unity using ultrathin metal layers.

Similar to distributed Bragg reflectors where the quarter-wave slabs are the key to the success of dielectric mirrors [32], we show in this paper that the ultra-thin metal films can be invisible to the incoming photons, leading to reflected-wave-cancellation and high transmission through the ultra-thin metallic films. Such a phenomenon is the key to the perfect absorption because the photons are absorbed by the ultra-thin metallic film without reflections. The phased ray-tracing analysis using an infinite series is conducted here, and we prove that the low reflectance and the high transmittance can indeed be achieved at the ultra-thin metallic film. Additionally, the accurate wave optics modeling result is presented to confirm the analytical result, and the same conclusion is arrived.

Finally, the experimental omnidirectionality for our proposed design using field penetration in moderately extinction metals is presented. Due to the physics of field penetration through the ultra-thin metallic film is, in fact, robust to the oblique incidence, the total broadband high absorbance can still be maintained at oblique incidence angles. This point will be explained in more detail in section 3.

2. Method and phased-ray analysis

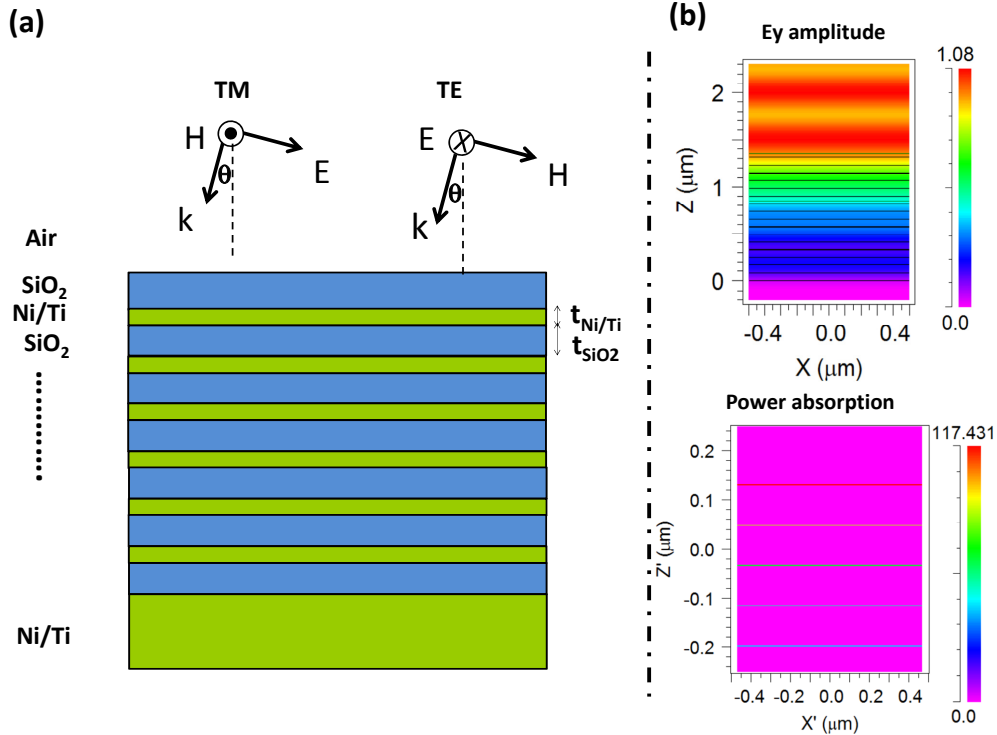


Fig. 1. (a) Illustration of the planar multilayer ultrathin metal MPA. (b) The field profile and the power dissipation at $\lambda = 1\mu\text{m}$. 16-pair (16X) Ni-based MPA. $t_{\text{Ni}} = 2\text{nm}$, $t_{\text{SiO}_2} = 80\text{nm}$. The field profile plots the amplitude of E_y at harmonic steady state. The power dissipation on the first five (topmost five) ultrathin metallic films is shown. The ultrathin metal layer requires very fine grid, i.e. 2.5\AA , to correctly resolve its power dissipation profile. 16-metal-layers in one plot exceeds the Rsoft's upper limit for display, and thus only the top 5-layer portion is shown.

The simulation is conducted using rigorously coupled wave analysis (RCWA). The material dispersion is from Rsoft material database [33]. The silicon dioxide (SiO_2) refractive index and extinction coefficient (n - k) are tabulated data for various wavelengths. The nickel (Ni) n - k is from an analytical expression using a Lorentz model. The measured n - k using an J.A. Woollam M2000 ellipsometer matches the Rsoft database well. In fact, the structure of multilayer planar MPAs using field penetration is not very sensitive to the material n - k due to it is a robust design. As a result, a slight deviation of material n - k due to different deposition methods is not an issue. Also, the design has robustness to the geometry variation from the process variation. For example, for the $\lambda = 400\text{nm}$ - 2000nm absorption range, t_{SiO_2} can range from 80nm to 150nm while the Ni-based MPA still provides a broad absorption band. In addition, it is worth to point out when t_{SiO_2} goes beyond 150nm , the absorption band can still exist for $\lambda = 400\text{nm}$ - 2000nm except some absorption dips in the spectral response. On the other hand, for the case of excessively-thin t_{SiO_2} , the insufficiently-spaced thin metallic layers leads to the situation where the bulk property of the metal becomes more pronounced instead of the ultrathin metallic film property. As a result, excessively-thin t_{SiO_2} is not desired. In short, when the metal film is thin enough, the number of pairs is sufficient for full absorption, and t_{SiO_2} is within the tolerance range, the broadband unity absorption can be achieved. Due to the above-mentioned reasons, the optimization algorithm for geometry selection is not necessary, and the proposed MPA design achieves a simple-design, simple-simulation, and simple-fabrication photonic device. Later we will show that the physics behind our ultrathin-

metal MPAs, and it will be clear that the satisfactory oxide spacer tolerance comes from the fact that the field penetration phenomenon does not significantly change with the dielectric spacer thickness for a wide range of photon energies and incident angles, provided the metal film is thin enough. Such physics leads to the realization of true ultra-broadband MPAs using a simple design. The experiment detail will be stated in section 4.

The device structure is plotted in Fig. 1(a). Alternating layers of Ni/SiO₂ is used in this study. Other metals and dielectrics can also be used without affecting the MPA characteristics if the metal extinction coefficient (k) is at a moderate level and facilitates field penetration. For the metallic thickness of 1nm to 2nm, which is the practical lower limit using e-gun evaporation, the k value below 5 is necessary to achieve MPA characteristics. Of course, for excessively low k such as $k < 1$, the MPA is still achievable, but the number of alternating pairs should be increased accordingly to achieve full absorption. The layer thickness t_{metal} and t_{SiO_2} will be stated in the figure captions for each simulation/experimental effort. The wavelength range in this study is visible to near infrared (NIR). The incidence angle is varying from 0° to 60° and both TE and TM results are presented. Essentially, the dependence on the photon polarization is quite weak for our proposed design. This is also due to the fact that the ultra-thin metallic film field penetration and reflected-wave-cancellation do not depend strongly on the photon polarizations. The field profile and the power absorption at harmonic steady state is plotted in Fig. 1(b). The gradually decayed electromagnetic field indicates that the absorption in the ultrathin metallic films is effective. The power absorption plot further confirms that the power absorption in the ultrathin metal films. It can be observed that the power absorption is the highest at the first metal film and then gradually decays at the subsequent metallic films underneath. This is correct because the optical power gradually decays with the penetration into the MPA, and therefore the power absorption is also declined accordingly.

3. The physics behind the broadband and omnidirectional nature: cancellation of the reflected rays

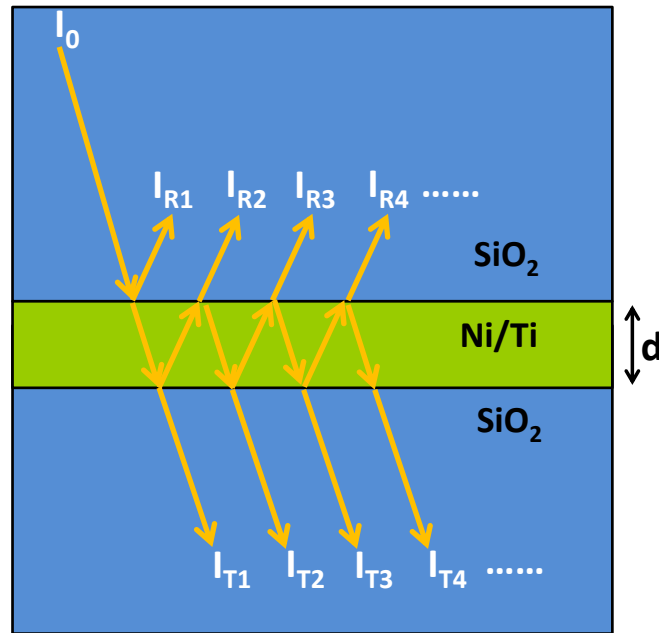


Fig. 2. Illustration of the field penetration at an ultrathin metallic film. The reflected/transmitted rays of different orders are added together to form total reflectance/transmittance. $I_{R1}, I_{R2}, I_{R3}, \dots$, are different reflection orders. $I_{T1}, I_{T2}, I_{T3}, \dots$, are different transmission orders.

The broadband and omnidirectional nature of proposed planar ultrathin metal MPAs can be analyzed in a more intuitive way using phased optical ray tracing. The technique is similarly employed for distributed Bragg reflectors (DBR) and leads to the conclusion that the quarter-wavelength slabs are necessary for a broadband high reflection. Other related photonic devices, such as Fabry-Perot interferometers and narrowband filters, can also be analyzed and designed using this technique. In this manner, the layer thickness and the arrangement of a quarter or half wavelength slabs may be known before performing full wave optics simulations [34, 35]. One thing to note is that the quasi-guided mode, plasmonic excitations, or diffraction grating is absent in our current design. This fact facilitates the broadband and omnidirectional nature. The reason is that the mode excitations can strongly depend on the wavelength and incident angles, evident from the photonic crystal theory [32]. The intersection of the line lines at a specific incidence angle and the photonic band structure determine the wavelength and the angle that provide quasi-guided mode excitation.

The ray tracing in our proposed ultrathin metal MPAs can be illustrated using Fig. 2. The thin metal is like a thin-film interferometer, and its thickness can affect the interference condition for the reflected rays. In order to know the total reflection at harmonic steady state, the infinite series of all reflected rays, I_{R1} , I_{R2} , I_{R3} , I_{R4} , ..., should be summed. The phase difference between these reflected rays I_{Ri} , comes from the optical path length inside the metal film and from the phase change by reflection and transmission. The phase change by reflection and transmission can be significant for metals due to the large imaginary part in their refractive indices. The sum of reflected rays can be written as,

$$\begin{aligned}
& I_{R,total} \\
&= \sum_i I_{Ri} = I_{R1} + I_{R2} + I_{R3} + I_{R4} + \dots \\
&= I_0 \Gamma_{Oxide2Ni} + I_0 T_{Oxide2Ni} \Gamma_{Ni2Oxide} T_{Ni2Oxide} e^{2kd} + I_0 T_{Oxide2Ni} (\Gamma_{Ni2Oxide})^3 T_{Ni2Oxide} e^{4kd} \\
&\quad + I_0 T_{Oxide2Ni} (\Gamma_{Ni2Oxide})^5 T_{Ni2Oxide} e^{6kd} + I_0 T_{Oxide2Ni} (\Gamma_{Ni2Oxide})^7 T_{Ni2Oxide} e^{8kd} + \dots \\
&= I_0 \Gamma_{Oxide2Ni} + I_0 T_{Oxide2Ni} T_{Ni2Oxide} \times \\
&\quad \left[\Gamma_{Ni2Oxide} e^{2kd} + \Gamma_{Ni2Oxide}^3 e^{4kd} + \Gamma_{Ni2Oxide}^5 e^{6kd} + \Gamma_{Ni2Oxide}^7 e^{8kd} + \dots \right] \quad (1) \\
&= I_0 \Gamma_{Oxide2Ni} + I_0 \Gamma_{Ni2Oxide} T_{Oxide2Ni} T_{Ni2Oxide} e^{2kd} \times \\
&\quad \left[1 + \Gamma_{Ni2Oxide}^2 e^{2kd} + \Gamma_{Ni2Oxide}^4 e^{4kd} + \Gamma_{Ni2Oxide}^6 e^{6kd} + \dots \right] \\
&= I_0 \Gamma_{Oxide2Ni} + I_0 \Gamma_{Ni2Oxide} T_{Oxide2Ni} T_{Ni2Oxide} e^{2kd} \frac{1}{1 - \Gamma_{Ni2Oxide}^2 e^{2kd}}
\end{aligned}$$

where I_0 is the incident ray, I_{Ri} is the i^{th} order reflection. Γ and T is the field amplitude reflection and transmission coefficients, and the subscript *Oxide2Ni* denotes the wave comes from the oxide to nickel, and *Ni2oxide* denotes the wave comes from nickel to oxide. k is the complex wave vector in metal, and d is the thickness of the ultra-thin metallic layer. It is illustrative if we examine the situation where the metal thickness becomes minuscule:

$$\begin{aligned}
& \lim_{d \rightarrow 0} I_{R,total} \\
&= \lim_{d \rightarrow 0} \sum_i I_{R_i} \\
&= \lim_{d \rightarrow 0} \left[I_0 \Gamma_{Oxide2Ni} + I_0 \Gamma_{Ni2Oxide} T_{Oxide2Ni} T_{Ni2Oxide} e^{2kd} \frac{1}{1 - \Gamma_{Ni2Oxide}^2 e^{2kd}} \right] \\
&= I_0 \Gamma_{Oxide2Ni} + I_0 \Gamma_{Ni2Oxide} T_{Oxide2Ni} T_{Ni2Oxide} \frac{1}{1 - \Gamma_{Ni2Oxide}^2} \\
&= I_0 \Gamma_{Oxide2Ni} + I_0 \Gamma_{Ni2Oxide} \left(\frac{T_{Oxide2Ni} T_{Ni2Oxide}}{1 - \Gamma_{Ni2Oxide}^2} \right) = I_0 \Gamma_{Oxide2Ni} + I_0 \Gamma_{Ni2Oxide} \\
&= I_0 \Gamma_{Oxide2Ni} - I_0 \Gamma_{Oxide2Ni} = 0
\end{aligned} \tag{2}$$

It can be concluded from Eq. (2) that as the metal film becomes ultra-thin, the reflection becomes negligible. Strictly speaking, if the metal layer thickness becomes close-to-zero, the transmittance will be close-to-one, the reflectance will be close-to-zero, and the absorbance will also be close-to-zero. In this case, a large number of metal-dielectric pairs is necessary for full absorption since a single metallic layer absorbs a minuscule amount of optical power. In practical application, several nanometer thickness is appropriate for low reflection and a reasonable amount of absorption in a single metal layer, for moderate-extinction metals such as Ti or Ni. The stacking of multiple metal layers leads to full absorption.

In the derivation in Eq. (2), we use the identity:

$$\frac{T_{Oxide2Ni} T_{Ni2Oxide}}{1 - \Gamma_{Ni2Oxide}^2} = 1 \tag{3}$$

The identity in Eq. (3) can be verified if we substitute the field reflection and transmission coefficient for T and Γ using the following expressions [32, 34, 35]:

$$\Gamma_{Oxide2Ni} = \frac{n_{oxide} - n_{Ni}}{n_{oxide} + n_{Ni}}, \quad \Gamma_{Ni2Oxide} = -\frac{n_{oxide} - n_{Ni}}{n_{oxide} + n_{Ni}} \tag{4}$$

$$T_{Oxide2Ni} = \frac{2n_{oxide}}{n_{oxide} + n_{Ni}}, \quad T_{Ni2Oxide} = \frac{2n_{Ni}}{n_{oxide} + n_{Ni}} \tag{5}$$

The field reflection and transmission coefficients can be derived using the boundary conditions for Maxwell's equations, and this can be found in the standard field and wave textbooks [32, 34, 35].

It can also be verified that at the ultra-thin metallic film thickness, the transmission will be close to I_0 :

$$\lim_{d \rightarrow 0} I_{T,total} = I_{T1} + I_{T2} + I_{T3} + I_{T4} + \dots = \lim_{d \rightarrow 0} = I_0 \tag{6}$$

Due to the paper length limitation, the derivation details are not shown here. The conclusion of vanished reflection, or equivalently unity transmission, is significant for the application of perfect absorption. In fact, such a conclusion is within expectation because when the layer thickness becomes much smaller than the wavelength, the photon cannot perceive the layer's presence. This feature leads to the situation where the photons can penetrate the thin metal films without perceiving them while a small amount of the optical power is dissipated during the process. Because only a small amount of optical power is dissipated in the ultrathin metal film, multiple layers are necessary to achieve full-absorption MPAs. It should be emphasized that the analysis here does not have strong wavelength dependence. As long as the ultrathin metal is used, the reflected wave cancellation exists for a broad range of photon energies. It is

not difficult to repeat the derivation in Eqs. (1)-(6) for oblique incidence with some modification in T and Γ in Eqs. (4) and (5) [32, 35]. It can be verified that as the metal film becomes ultrathin, minimal reflection can be achieved at oblique incidence. As a result, broadband and omnidirectional MPA is realized.

Figure 3 plots the realistic situation using RCWA wave-optics simulation, and the results confirm our phased-ray-tracing conclusion. A thin layer of Ni film is placed in SiO₂ background, and the reflectance (R), the transmittance (T), and the absorbance (A) are calculated. The transmittance, absorbance, and reflectance is calculated over a broad wavelength range. Figure 3 plots the situation for 2nm and 1nm Ni film. It can be seen that the reflection is negligible. The absorption is around 0.2 for 2nm thick Ni film and 0.1 for 1nm thick Ni film, and thus, 10 pairs of Ni/SiO₂ should be enough for full absorption. Reduced Ni thickness is beneficial for the purpose of MPAs, which is evident from comparing Figs. 3(a) and 3(b). It can be observed that as the Ni thickness is decreased, the situation becomes more similar to the phased ray tracing analysis in Eqs. (1)-(6). For oblique incidence, the perfect absorption is robust to the incidence angle, evident from Figs. 3(c) and 3(d) for the case of 60° TE and 60° TM incidences. The physical reason for the decent angular response is due to the fact the phenomenon depicted in our phased ray tracing analysis does not strongly depend on the incidence angle. At oblique incidence, the vanished reflection at an ultrathin metal film thickness is still present, provided the metal film thickness be thin enough for a particular oblique incidence angle. The effective optical path length inside the metal films can be longer for oblique incidence, and thus thinner metal films are preferred for wide-angle MPAs. Nevertheless, thinner metal films inevitably require more pairs of metal/dielectric stacking. The derivation from Eqs. (1)-(6) can, in fact, be reproduced for oblique incidence with some modification in the expression of T and Γ in Eqs. (4) and (5) [32, 35].

Finally, we want to point out that the reflected-wave cancellation is achieved with a single ultrathin metal film, as derived in this section. This leads to a satisfactory tolerance in the dielectric spacer thickness selection. In contrast, if the reflected wave cancellation counts on the destructive interference between the reflected waves by the adjacent metallic films separated by dielectric spacers, the dielectric space thickness can dramatically change the interference condition. In our design, the ultrathin metal film provides reflected wave cancellation by itself and, therefore, relaxes the constraint on dielectric spacer thickness selection.

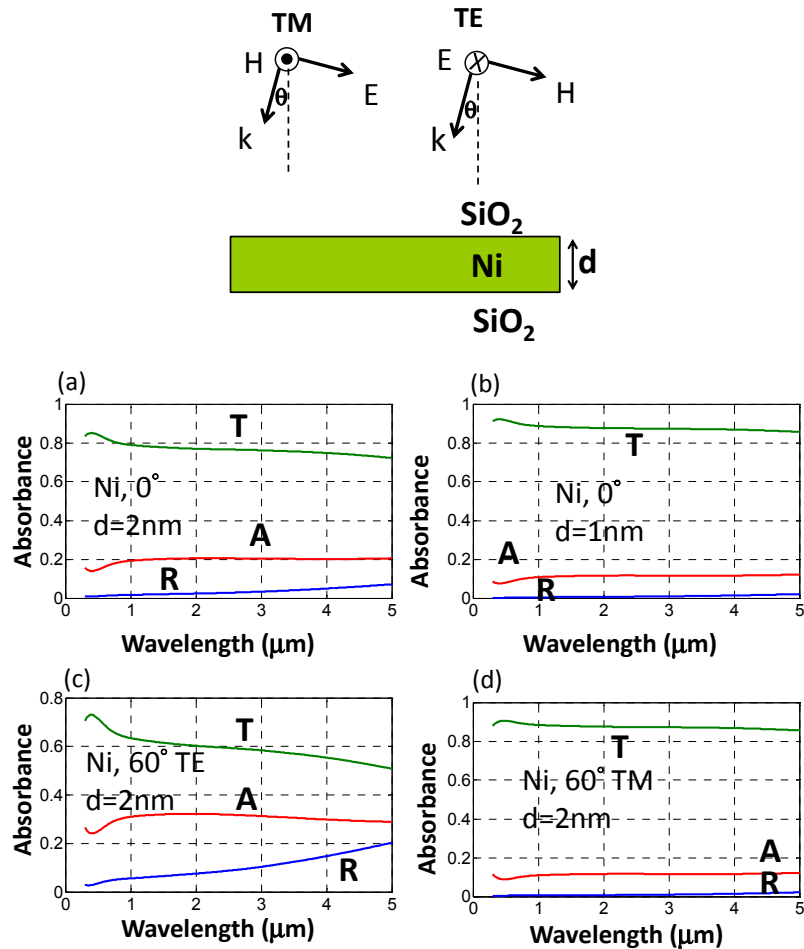


Fig. 3. Full-wave calculation using rigorously coupled wave analysis (RCWA). The transmittance (T), reflectance (R), and absorbance (A) for an isolated metallic film (Ni). The background is assumed to be SiO₂. The metal film thickness (d) is specified in the figure.

4. Experiment

A 200nm Ni or Ti layer is deposited on a bare silicon wafer. Afterward, 16 pairs of Ni/SiO₂ or Ti/SiO₂ alternating layers are deposited sequentially. The deposition of the Ni-based MPAs is done with AST PEVA 600I electron gun (e-gun) evaporators. The deposition of SiO₂, Ni, and Ti films is conducted at 5×10^{-6} , 3×10^{-6} , and 3×10^{-6} torr, respectively, without substrate heating. The deposition rate for e-gun evaporation is 0.1nm/sec for Ni, 0.5nm/sec for Ti and 0.2nm/sec for SiO₂. Further optimization of the surface roughness and thin film morphology is possible with the adjustment of the deposition pressure and rate. For a fully smooth film, the metalorganic chemical vapor deposition, molecular beam epitaxy, or atomic layer deposition can be employed. For 1nm Ni MPAs, the deposition of Ni using e-gun evaporator has to be done in different runs. This is because the Ni deposition rate is gradually increased with the number of deposited pairs due to the heating of the target. This results in more difficulty to control the thickness to the ultra-thin dimension of 1nm. Therefore, we break the 16-pair deposition of the 1nm-Ni MPA into several runs to let the target cool down. The measurement configuration of the normal incidence absorbance using Hitachi U-4100 is illustrated in Fig. 4.

The normal incidence data is plotted in Fig. 5, for different Ni-based or Ti-based MPAs. The surface roughness data is measured by using atomic force microscope (AFM) and shown in Fig. 6. No polarizer is installed for the measurement in Fig. 5, and thus all polarizations exist. It can be seen in Fig. 5 that although 1nm Ni MPAs should, in theory, have the better response than 2nm Ni, the measured data is worse than 2nm Ni MPA. This is because the 1nm Ni film is too thin, and the excessively short e-gun deposition time can affect the initial nucleation. Using e-gun to deposit 1nm Ni with the current deposition rate of 0.2nm/sec does not provide a decent film. On the other hand, 2nm Ni-based MPAs have satisfactory spectral absorbance, providing close-to-unity ultra-broadband absorption. 2nm Ti MPA should also, in theory, exhibit decent broadband absorbance. Nonetheless, large ripples exist over the entire absorption band. Ti, in fact, has a better n-k matching, as far as the purpose of perfect absorbers is concerned. Ni extinction (k) is slightly higher than Ti, for the wavelength range from visible to near infrared. Nevertheless, in practice when using e-gun evaporator, Ti film thickness is more difficult to control, and overgrowth is very likely to happen especially at the end of 16-pair deposition due to the heated Ti target. This is potentially due to the higher melting point of Ti compared to Ni. For 2nm Ni with 30nm oxide spacer, the calculated response shows decayed absorption for wavelength $>1\mu\text{m}$. In the AFM measurement of the fabricated samples, the RMS surface roughness $\sim 3\text{nm}$ in the Ni samples results in pronounced near-field enhancement for wavelength $>1\mu\text{m}$. Therefore, the experimental absorption is elevated. It should be emphasized that the surface roughness of several nanometer range does not lead to far-field effect. This is evident from comparing the normal incidence absorbance result with integration sphere, demonstrated in Figs. 4 and 5, and the nearly-normal (10°) absorbance result without integration sphere, demonstrated in Figs. 7 and 8. The close similarity between the 10° data in Fig. 8 and the normal data in Fig. 5 supports the fact that the nanometer range surface roughness in our sample does not lead to any noticeable far-field non-specular diffraction orders. We believe the broadband MPA characteristics, which we demonstrate here experimentally, is the closest to the broadband unity absorption, compared to the earlier important effort in the literature [36, 37].

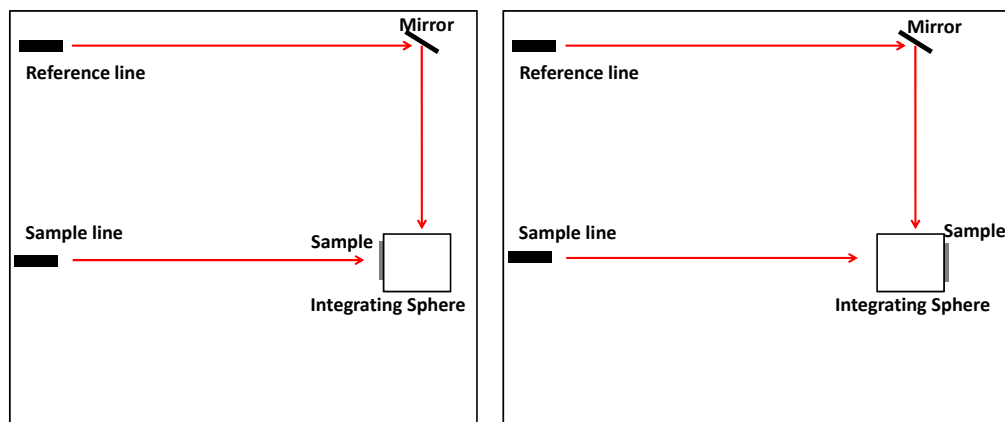


Fig. 4. The measurement setup for normal incidence spectral absorbance. No polarizer is installed, and thus all polarizations exist. (Left) The setup for transmittance (T). (Right) The set-up for reflectance (R). Absorbance (A) is $1-T-R$. Integration sphere is used in this setup.

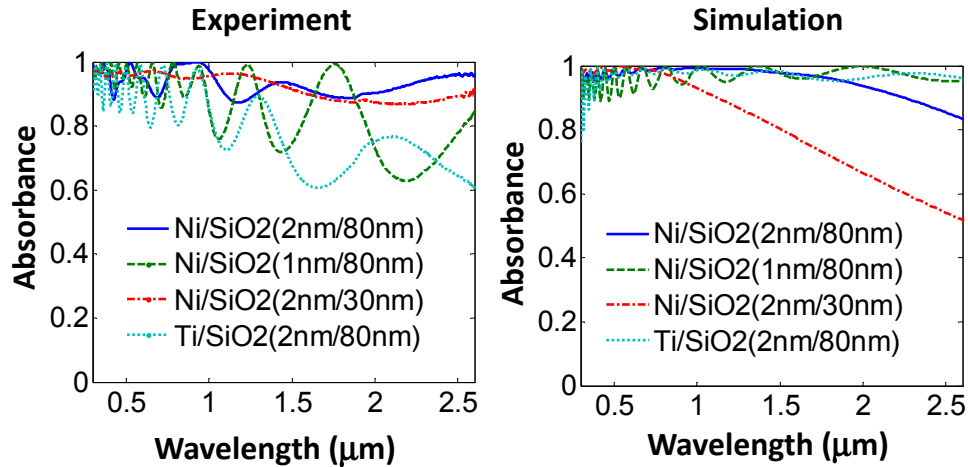


Fig. 5. The measured spectral absorbance for normal incidence (0°). 16-pair (16X) Ni/SiO₂. The thicknesses of metal and dielectric are labeled in the caption. No polarizer is installed, and thus all polarizations exist.

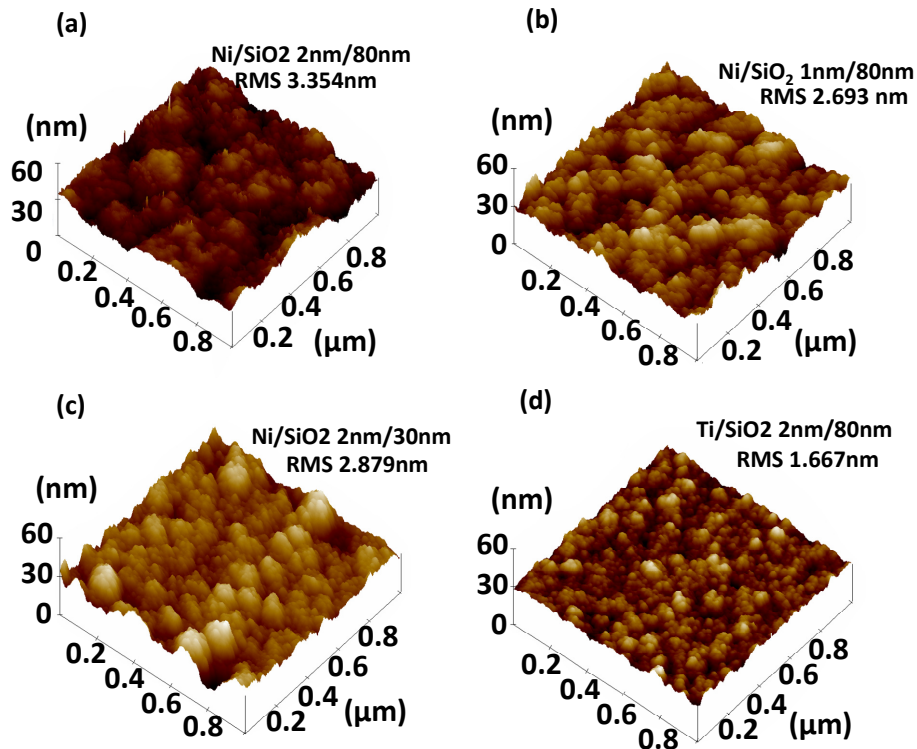


Fig. 6. The atomic force microscope (AFM) image of the samples in Fig. 5. The top surface of the 16-pair (16X) stack is measured by AFM. RMS roughness values are shown beside the micrographs. The substrate is a silicon wafer with a 200nm metallic bottom plate.

Due to the 2nm-Ni/80nm-SiO₂ MPA has close-to-unity absorbance, we use the sample to demonstrate the angular response and omnidirectionality. The measurement setup is illustrated in Fig. 7. The experimental result for angular measurement is still conducted using

Hitachi U-4100 with variable angle assembly P/N 134-0116. The TE and TM incidence are accomplished using a polarizer. Figure 8 shows the absorption at oblique incidence angles from 10° to 60° . The broadband absorption does not significantly vary with polarizations and incidence angles. The physics has been explained using phased ray tracing analysis in section 3. Due to the physics, i.e. the field penetration and the reflected wave cancellation at the ultrathin metal, is robust to wavelength, incidence angle, and polarization in our proposed design, the broadband absorption will not vanish for variable incidence angles and polarizations. It can be seen that the TM polarization has higher performance compared to TE polarization, especially at 60° incidence angle. This is due to the lower reflectance for TM polarizations at the metal-oxide interface for oblique incident angles. It is well known that Brewster angle (θ_B) only exists for TM polarized light. As a result, the TM angular reflectance is lower than TE for most material interfaces. The last thing to point out is that the absorbance at the nearly normal directions (10°) in Fig. 8 is quite the same as the normal incidence absorbance using integration sphere in Fig. 5, indicating the far-field non-specular power is absent. This is reasonable since the structure here is planar. It should be mentioned again that although in the setup in Fig. 7, only the specular component of T and R is measured, it equals the total T and R due to the planar geometry. In addition, the surface roughness of our sample is only several nanometer, which is not sufficient to lead to any far-field non-specular diffractions. As a result, the absorbance in Fig. 8 can be regarded as accurate total absorbance. This point can be confirmed by noticing the close similarity between the normal data in Fig. 5 and the 10° data in Fig. 8, where integration sphere is present in Fig. 5 but absent in Fig. 8.

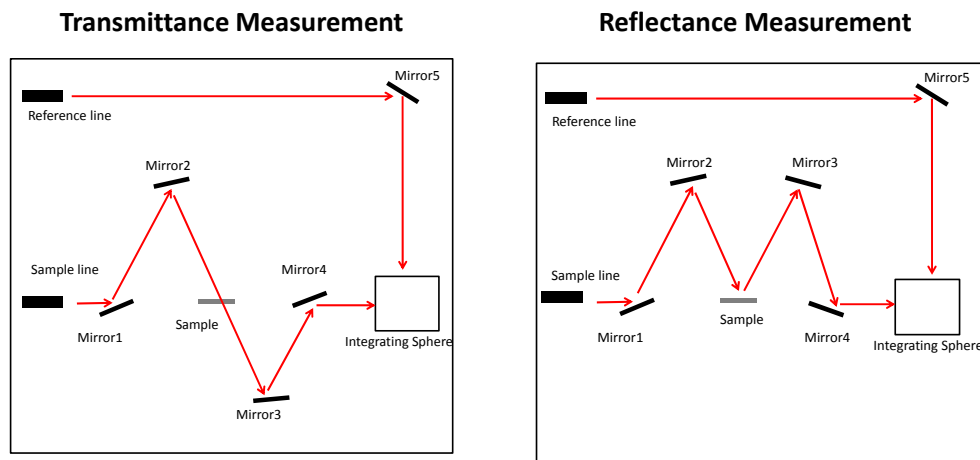


Fig. 7. The measurement set-up for the oblique-incidence specular reflectance/transmittance. Integration sphere is not directly attached to the sample, and thus, only specular reflectance/transmittance is collected. Nevertheless, the specular reflectance/transmittance **equals** total reflectance/transmittance due to the planar multi-layer structure. (Left) The setup for transmittance (T). (Right) The measurement set-up for reflectance (R). Absorbance (A) is $1-T-R$.

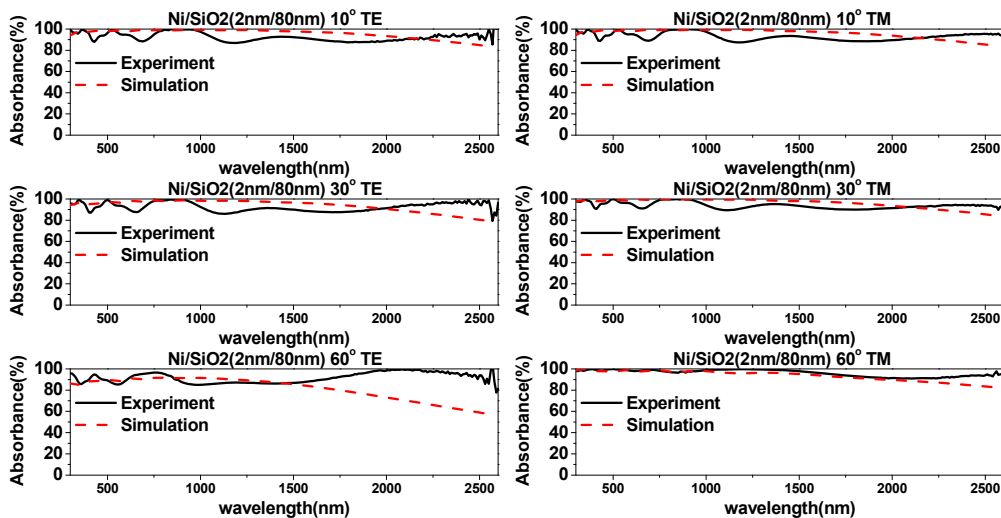


Fig. 8. The measured spectral absorbance for TE and TM polarizations until 60°. 16-pair (16X) Ni/SiO₂. $t_{\text{Ni}} = 2\text{nm}$. $t_{\text{SiO}_2} = 80\text{nm}$. Absorbance (A) is 1-transmittance(T)-reflectance(R). The T and R are measured using the setup in Fig. 7. The specular T and R is measured in this case. Nevertheless, due to the planar geometry, the specular power is equal to the total power. In these samples, the measured T is zero due to the 200nm Ni bottom plate.

To further confirm the superior omnidirectionality of our proposed MPAs, we use another configuration to measure its angular response, illustrated in Fig. 9. In this measurement, the sample is placed in an integration sphere, and in this case, both specular and non-specular reflectance and transmittance are collected by the integration sphere. The wavelength measurement range of this integration sphere system is $\lambda = 400\text{nm}$ to $\lambda = 1000\text{nm}$ due to the fact that it is a solar cell angular measurement system. In fact, the planar structure has no diffraction and thus no integration sphere is necessary. An Ocean Optics QE65000 spectrometer and a Xe lamp are used. No polarizer is installed, and thus all polarizations exist. The measured spectral absorption for various incidence angles is shown in Fig. 10.

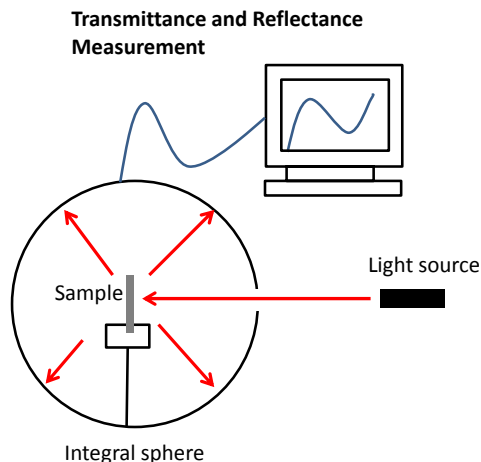


Fig. 9. The measurement set-up for the total transmittance and total reflectance. The transmitted and reflected rays are summed together using integration sphere. In fact, the transmittance is zero for this sample due to 200nm Ni bottom plate. The wavelength measurement range of this integration sphere system is $\lambda = 400\text{nm}$ to $\lambda = 1000\text{nm}$. No polarizer is installed, and thus all polarizations exist.

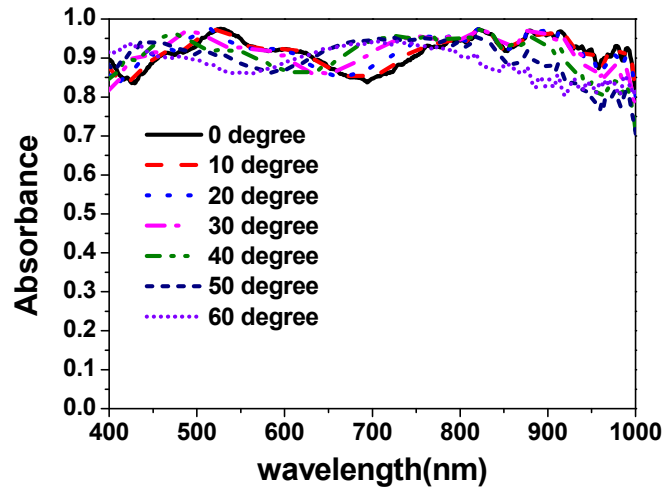


Fig. 10. The measured total absorbance for 16X Ni/SiO₂ with $t_{\text{Ni}} = 2\text{nm}$, $t_{\text{SiO}_2} = 80\text{nm}$. No polarizer is installed, and thus all polarizations exist. Absorbance (A) is 1-transmittance(T)-reflectance(R). The wavelength measurement range of this integration sphere system is $\lambda = 400\text{nm}$ to $\lambda = 1000\text{nm}$.

5. Conclusion

In this work, we present an analysis model that pinpoints the key physics behind the ultra-broadband and omnidirectional nature of the field-penetration MPAs. The infinite series, for the reflected and transmitted rays of different-orders, reveal that the reflection at the ultra-thin metal film can be made minimal provided the film thickness is much smaller than the skin-depth of the metallic material. Similar to the quarter-wavelength slabs for DBRs, the ultrathin metal film thickness is identified as the key part for broadband omnidirectional perfect absorption. At ultrathin metal thickness, the field penetration and the reflected wave cancellation phenomenon will not change significantly with wavelength, incident angle, and polarization. This point is verified by an analytical model using series technique and wave-optics RCWA calculation. More importantly, the angular response for both TE and TM polarizations is measured for the proposed MPAs, and the ultra-broadband absorption can be sustained until 60 degrees. The detailed measurement with or without integration sphere, at various incident angles for UV-VIS-NIR wavelength range, is presented. The result confirms that the physics of field-penetration and reflected-wave-cancellation are robust to wide incidence angles. We think the proposed omnidirectional, polarization-independent, and ultra-broadband MPAs can be very promising for future nano-photonics applications.

Acknowledgments

The work is supported by the Ministry of Science and Technology (MOST), Taiwan, under fund number MOST-104-2221-E-009 -115 -MY2.